batteries

MDPI

Article

An Electrical–Thermal Coupling Model with Artificial Intelligence for State of Charge and Residual Available Energy Co-Estimation of LiFePO4 Battery System under Various Temperatures

Shuoyuan Mao [1], **Meilin Han** [1], **Xuebing Han** [1,*], **Languang Lu** [1], **Xuning Feng** [1], **Anyu Su** [1], **Depeng Wang** [1], **Zixuan Chen** [2], **Yao Lu** [1] and **Minggao Ouyang** [1,*]

[1] State Key Laboratory of Automotive Safety and Energy, Tsinghua University, Beijing 100084, China
[2] School of Aerospace Engineering and Applied Mechanics, Tongji University, Shanghai 200092, China
* Correspondence: hanxuebing@tsinghua.edu.cn (X.H.); ouymg@mail.tsinghua.edu.cn (M.O.)

Abstract: The LiFePO4 (LFP) battery tends to underperform in low temperature: the available energy drops, while the state of charge (SOC) and residual available energy (RAE) estimation error increase dramatically compared to the result under room temperature, which causes mileage anxiety for drivers. This paper introduces an artificial intelligence-based electrical–thermal coupling battery model, presents an application-oriented procedure to estimate SOC and RAE for a reliable and effective battery management system, and puts forward a model-based strategy to control the battery thermal state in low temperature. Firstly, an LFP battery electrical model based on artificial intelligence is proposed to estimate the terminal voltage, and a thermal resistance model with an EKF estimation algorithm is established to assess the temperature distribution in the battery pack. Then, the electrical and thermal models are coupled, a closed-loop EKF algorithm is employed to estimate the battery SOC, and a fusion method is discussed. The coupled model is simulated under a given protocol and RAE can be obtained. Finally, based on the electrical–thermal coupling model and RAE calculation algorithm, a preheating method and constant power condition-based RAE estimation are discussed, and the thermal management strategy of the battery system under low temperature is formed. Results show that the estimation error of SOC can be controlled within 2% and RAE can be controlled within 4%, respectively. The preheating strategy at low temperature and low SOC can significantly improve the energy output of the battery pack system.

Keywords: LFP battery; SOC; RAE; electrical–thermal coupling; low temperature

check for updates

Citation: Mao, S.; Han, M.; Han, X.; Lu, L.; Feng, X.; Su, A.; Wang, D.; Chen, Z.; Lu, Y.; Ouyang, M. An Electrical–Thermal Coupling Model with Artificial Intelligence for State of Charge and Residual Available Energy Co-Estimation of LiFePO4 Battery System under Various Temperatures. *Batteries* **2022**, *8*, 140. https://doi.org/10.3390/batteries8100140

Academic Editor: Juan Carlos Álvarez Antón

Received: 18 August 2022
Accepted: 19 September 2022
Published: 22 September 2022

1. Introduction

1.1. Backgrounds

Electrification of the automobile is considered the future trend of vehicles in the environmental corporation community [1,2]. Lithium-ion battery (LIB) has become the ideal power supply for electric vehicles relying on its high energy density, high security and long service life [3,4]. Owing to the high stability and low price, LFP is being widely used as a cathode material [5,6]; according to the official statistics, the installed capacity of the LiFePO4 battery has accounted for more than half of the total capacity in China by 2021.

Nevertheless, LIB suffer from a serious energy attenuation problem in low temperature, especially LFP batteries [7,8]. Qin et al. reviewed the performance of batteries at low temperature and illustrated that the discharge capacity of LFP drops from 134.5 mAh/g (20 °C) to 90 mAh/g (−20 °C) [9], which corresponds to the authors' pre-experiment, as shown in Supplementary Material Figure S1.

The performance degradation of LIB at low temperature is mainly caused by the increase in electrolyte viscosity, the decrease in the electrode solid diffusion coefficient and increase in solid electrolyte interface impedance [9,10]. These physical properties lead to the LIB exterior characteristic of resistance increase and make the available energy of the battery drop significantly.

To relieve the range anxiety of electric vehicle owners at low temperature, the RAE should be estimated accurately to show the true energy state of the vehicle to the users, which has been a problem in the industrial and academic community, especially for LFP batteries at low temperature. Firstly, the SOC of an LFP battery is difficult to accurately estimate for its voltage characteristics. Secondly, limited temperature measurement points of the battery module and magnification of the cell-to-cell temperature variation at low temperature increase the state estimation difficulty. Thirdly, the state of energy (SOE) is used to represent the energy condition of the battery, which often has a linear mapping relationship with SOC in practical application, but the mapping becomes inaccurate at low temperature for the aforementioned reasons.

Indicating to improve the LFP battery module charge state and energy state estimation accuracy at low temperature, this research breaks the complex problem into three parts: accurate SOC estimation of LFP battery, simplified battery module thermal model and estimation of module temperature distribution, and RAE estimation of battery module. Most remarkably, the method proposed in this research is also applicable to LIBs of other material systems in the full temperature range.

1.2. Literature Review

1.2.1. State of Charge

The definition of SOC is called the Coulomb counting method, which is described by Equation (1).

$$\mathrm{SOC} = \mathrm{SOC}_0 - \frac{1}{C_{bat}} \int_{t_0}^{t} \eta I \cdot d\tau \tag{1}$$

where SOC_0 is the initial SOC when the calculation is started, C_{bat} is the standard capacity of the battery tested at a C rate of 1/3 and temperature of 25 °C, η is the columbic efficiency, and I is the current.

Hence, SOC reflects the remaining charge of the battery at standard state, which would not be influenced by temperature, and that is the significant difference between SOC and SOE/RAE.

To correct the accumulative estimation error brought by sensor error and battery aging, scientists proposed model-based closed-loop SOC estimation algorithms. The electrochemical mechanism models can accurately reflect the true internal state and external characteristics of the battery; however, the computational complexity is too high to be applied on BMS [11]. Wu et al. proposed a novel improved reduced-order electrochemical model, which has both high model fidelity and less computational complexity [12]. Liu et al. introduced a single particle model-based nonlinear observer to monitor SOC [13]. Another most commonly used battery model is the equivalent circuit model (ECM), such as Rint model (0 order), Thevenin model (1st-order) and double polarization model (2nd-order) [14]. With the battery model, a closed-loop state estimation algorithm based on modern control theory are often applied to improve SOC estimation accuracy. Extended Kalman filtering (EKF) and particle filter (PF) algorithms are the most commonly used algorithms, which achieve good results in the former studies [15–17].

However, the ECM-based SOC estimation method is not completely suitable for an LFP battery, since the algorithms require the open circuit voltage (OCV) to SOC curve of the battery, and the OCV-SOC curve of an LFP battery has three segments that are very flat, as shown in the Supplementary Figure S2. The platform area of the LFP battery caused a significant error increase at the posterior estimation process [18–20].

To overcome the poor SOC estimation accuracy problem of an LFP battery, Huria et al. proposed an ECM with a hysteresis effect, bringing a slope to the actual OCV curve. This method can alleviate the problem but could not solve the problem fundamentally. Duong et al. designed an algorithm to restructure the OCV curve of an LFP battery at varying temperatures [19]. Xiong et al. put forward a theory to update all of the parameters including OCV, capacity, resistances and capacitances in ECM for all-climate batteries [21]. These methods can achieve a higher accuracy of the model elements but still cannot overcome the OCV characteristics problem of LFP.

On the other hand, the NN-based terminal voltage modeling method can totally avoid the platform problem of an OCV curve, and theoretically, it can achieve higher SOC estimation accuracy for the LFP battery. Chen et al. built an improved battery model by introducing an input reflecting the characteristics of polarization [22], and the result shows that the SOC estimation error of an NCM battery can be stabilized within 2% at different temperatures. However, the NN-based method has not been applied to the modeling process of an LFP battery to solve the plateau problem, and the modeling accuracy should be verified.

1.2.2. Battery Module Thermal Model

The cell-to-cell temperature variations of a power battery in electric vehicles cannot be ignored; in cold weather, due to the deterioration of heat generation and heat dissipation, the module temperature inconsistency would be enhanced [4,23–25]. To control the production cost, the battery module and electric vehicle manufacturer tend to arrange a few temperature sensors on the module, which makes the cells without temperature sensors under monitored. To estimate the energy state of the module accurately, it is necessary to know the temperature of each cell; thus, the battery module thermal model is studied.

The finite element method or finite volume method-based battery thermal model can accurately obtain the battery temperature field distribution, and these are widely used in the battery thermal simulation area, but the calculation amount is too large to be applied in a BMS [26–28]. On the other hand, the lumped parameter model only takes the average temperature of the battery into account; thus, it has high computational efficiency and is applicable to a BMS. The method to avoid oversimplification of the lumped model is to divide the cell into several parts. Hua et al. delivered a lumped 3D battery thermal model with a network of electric and thermal sub-models, exchanging the temperature and heat generated in each of the discretized volumes [29]. Jiang et al. built a two-state lumped thermal resistance model of the single cell and connected it to a network of the LIB pack; the prediction of battery core temperature agrees well with the measurement [30]. Cui et al. proposed and compared two-state, five-state and improved five-state lumped parameter thermal models of prismatic battery, and they found that the lumped parameter model is practical for online battery internal temperature estimation [31]. To build a battery system thermal model with low complexity and high accuracy, the lumped parameter model should be considered, and the closed-loop temperature estimation method could be applied.

1.2.3. Residual Available Energy

The state of energy is often used to reflect the available energy condition of the battery, and it is considered better than SOC in this respect [32–34]. Mamadou et al. defined an SOE for the first time [35], and the commonly used definition of SOE is shown in Equation (2) [36].

$$\mathrm{SOE} = \frac{\mathrm{RAE}\ |_{I,T,\mathrm{SOC},SOH}}{\mathrm{MAE}\ |_{I,T,SOH}} \times 100\% \tag{2}$$

where MAE is the value of the maximum available energy of the battery, RAE is the value of the residual available energy of the battery, and SOE is the ratio of RAE to MAE. As can be seen from the formula, RAE is a function of the battery current, temperature, SOC and *SOH*, while MAE is a function of the battery current, temperature, and *SOH*. Thus, SOE can be influenced by all these parameters—that is a main difference between SOE and SOC. As illustrated in Section 1.2.1, SOC would not be influenced by the ambient temperature: for example, if a battery is simply moved from a high-temperature environment to a low-temperature environment, the SOC would not change, but the SOE would change significantly. That can also prove that the SOE has a better ability to reflect the true discharge capability of the battery.

The actual energy state estimation of a battery has not been well solved at present. Some early researchers thought SOE and SOC have a linear relationship [37], which is not accurate under dynamic load and various temperature and is not suitable for an LFP battery. Many researchers used closed-loop model-based SOE estimation methods exactly as an SOC estimation process [33,38–42], but these methods all use an OCV-SOE curve to determine the battery SOE; thus, they have no difference with the SOC-SOE mapping method. Li et al. demarcated RAE under various temperature, current and aging conditions [36], and the mapping method has good performance but needs massive testing experiments. Liu et al. first proposed an NN-based SOE estimation method [43], but it is more difficult for this to be accurate than NN-based SOC estimation because of the more complex influencing factors. Furthermore, fewer researchers have focused on the energy state estimation of the whole battery module or the electric vehicle.

German et al. proposed a method to directly simulate the remaining driving range of electric vehicles [44]. However, the characteristics of the battery cannot be reflected well; thus, the method is unable to maintain accuracy in various conditions. Consequently, a method to determine the RAE of the battery system should be developed without the mapping between OCV and SOE to accurately reflect the battery energy state, especially in low temperature.

1.3. Contributions of this Research

To overcome the existing problems in SOC and SOE estimation of the LFP battery module especially under low temperature, this research is dedicated to introducing a high-precision solution to a practical application of BMS, and it has the following three commendable contributions:

We proposed an NN battery model-based closed-loop SOC estimation method of an LFP battery, which can avoid the platform problem of an OCV curve. Further, we performed a fusion method to reduce the computational complexity and increase the robustness.

We built a thermal resistance network of the battery module with a two-state lumped parameter battery thermal model, and we used the closed-loop method to obtain the temperature distribution of the battery module based on a limited number of temperature sensors.

We calculated the RAE of the battery module under a given test condition at various SOCs and temperatures, and we discussed the preheating strategy performance.

1.4. Organization of this Paper

The paper is organized as follows: Section 2 introduces the construction of the electrical and thermal model of the battery. Section 3 proposes the experiments to identify the parameters and to verify the models. The electrical and thermal models are combined and simulated, SOC and RAE are obtained, and then analysis and discussion are provided in Section 4. Finally, the conclusions are summarized in Section 5.

2. Methodology

This section proposed a novel NN-based LFP battery model. Then, the battery thermal model is built, and the EKF algorithm is applied.

2.1. Battery Electrical Model

The traditional ECM is a model regarding the battery as a series–parallel combination of circuit elements including voltage source, resistance, inductance, etc., to simulate the terminal voltage of the battery. To make a comparison study, a 2nd-order ECM is built in the study, as shown in Figure 1a.

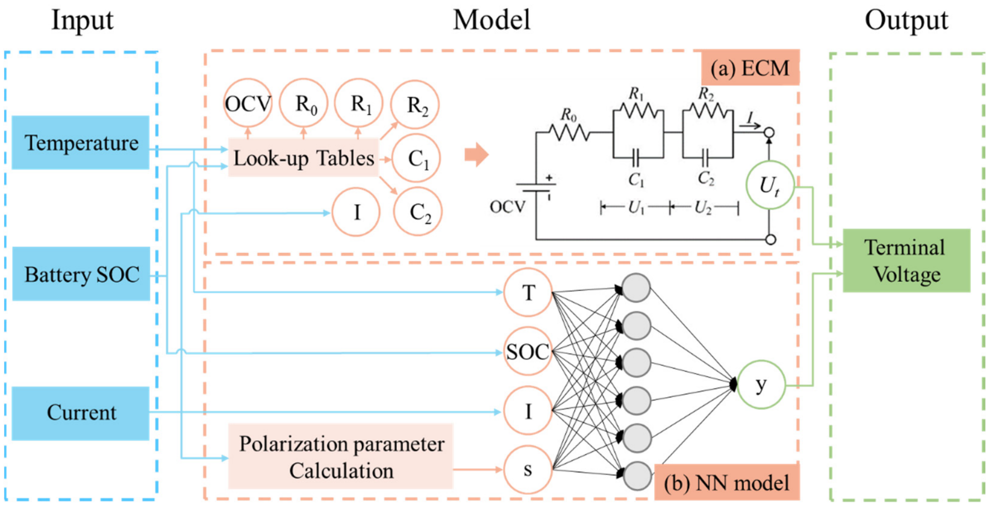

Figure 1. Battery models. (**a**) 2nd-order ECM. (**b**) NN model.

Different from electric circuit modeling methods that rely on physical processes, machine learning does not depend on the understanding of the physics essence, but it can automatically establish the mathematical relationship between the input and output from a large amount of data, which is suitable for describing the nonlinear characteristics of batteries [45]. In this study, the authors proposed a neural network (NN)-based LFP battery model, which can directly model the terminal voltage of the battery without using OCV. The authors found that although there are platform areas in the OCV curve of LFP, the terminal voltage under dynamic condition is not as flat as the OCV curve. As shown in Figure S3, the voltage range of the OCV curve in the platform area is about 1 mV, while that of terminal voltage under the FUDS test condition is at 10 mV magnitude, and that range can be detected by the commercial voltage sensor. The authors conjecture that phenomena is caused by the polarization of the battery under applied dynamic current. In order to build an accurate NN battery model suitable for all temperatures, the temperature, SOC, current, and polarization parameter [22] are used as the input feature vector of the neural network, and the terminal voltage is set as the output of the NN model. As shown in Figure 1b, the input s represents the polarization parameter, and a more detailed illustration of that parameter is shown in the supplementary file. The network is constructed of one input layer with four input nodes, one hidden layer with six hidden nodes and one output layer with one output node, which is relatively simple and makes the feedforward calculation and subsequent closed-loop calculation process easy to be performed.

The formula of the NN model is shown in Equation (3):

$$\mathrm{y} = W_2 \times tansig(W_1 \times \mathrm{x} + b_1) + b_2 \tag{3}$$

where y is the output and x is the input of the NN model, W_1 and W_2 are the weight matrixes, b_1 and b_2 are the bias vectors, and *tansig* (*) is the nonlinear function in the hidden layer.

2.2. Battery Thermal Model

The aim of building a battery system thermal model is to estimate the temperature of batteries without temperature sensors, especially the batteries with the lowest and highest temperature, which are the limitations of the battery module discharge and charge ability. In this study, a two-state lumped parameter thermal model is constructed as the single cell model, the EKF algorithm is introduced as the closed-loop method to estimate the battery core temperature, and a network of single cells is connected to form the module model. The modeling is based on the battery pack of Wuling HongGuang Mini EV (SAIC GM Wuling Automobile Co., Ltd., Liuzhou, China) [8].

2.2.1. Single Cell Thermal Model and EKF Algorithm

The so-called "two-state" refers to the abstraction of the entire cell into two mass points of "core" and "shell", as shown in Figure 2a. The basic thermal parameters of each part are shown in Table S1.

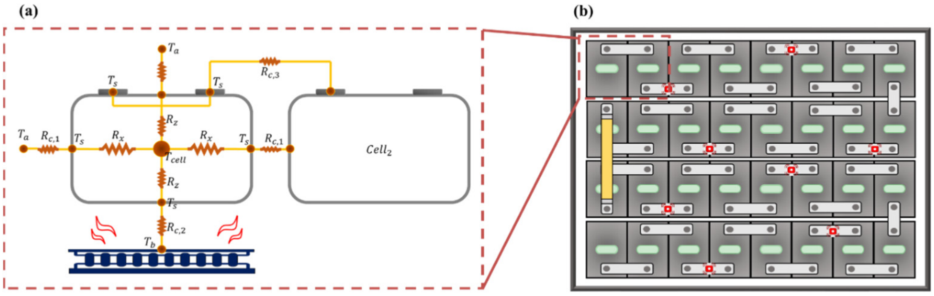

Figure 2. The thermal model of the battery and module. (**a**) Single battery model. (**b**) Battery module model.

The two-state lumped parameter model assumes heat is generated from the core. Then, the heat transfer from the core to the shell, the shell and environment follow a convection cooling process.

The heat generation of the core includes reversible heat and irreversible heat, as shown in Equation (4):

$$\begin{cases} q = q_{rev} + q_{irr} \\ q_{rev} = -IT\frac{\partial U_{OCV}}{\partial T} \\ q_{irr} = I^2R \end{cases} \tag{4}$$

where q_{rev} is the reversible heat. To calculate q_{rev}, the entropy heat coefficient needs to be identified, which is the calculation by partial derivative OCV with respect to temperature T, q_{irr} is the irreversible heat and is needed to identify the total resistance R which is calculated by voltage drop at small C rate divided by the current. The map of heat production parameters is shown in Figure S4.

The heat transfer equation from the battery core to the shell is shown in Equation (5): where c_{core} is the specific heat capacity of the core, q is the heat generation, T_{core} is the core temperature, T_s is the shell temperature, and R_{core2s} is the equivalent thermal resistance of heat transfer from core to shell, in K/W. The calculation method of R_{core2s} is to abstract the heat conduction in three directions inside the battery into three thermal resistances, and the three thermal resistances are connected in parallel to calculate the total thermal resistance, as shown in the second formula in Equation (5). The thermal resistance in each direction is calculated by dividing the thickness by the thermal conductivity in that direction, as shown in the third formula in Equation (5).

$$\begin{cases} c_{core}\frac{\Delta T_{core}}{\Delta t} = q - \frac{T_{core}-T_s}{R_{core2s}} \\ \frac{1}{R_{in2s}} = \frac{1}{R_{xx}} + \frac{1}{R_{yy}} + \frac{1}{R_{zz}} \\ R = \frac{\delta}{\lambda} \end{cases} \tag{5}$$

The process of convection heat dissipation from the shell to the environment is also abstracted as a thermal resistance model, as shown in Equation (6): where c_s is the specific heat capacity of the shell, T_{out} is the ambient temperature outside the cell, R_{s2out} is the equivalent thermal resistance of heat transfer from the shell to environment, as calculated in the second formula in Equation (6), in which h is the convective heat transfer coefficient and A is the heat exchange area.

$$\begin{cases} c_s\frac{\Delta T_s}{\Delta t} = \frac{T_{core}-T_s}{R_{core2s}} - \frac{T_s-T_{out}}{R_{s2out}} \\ R_{s2out} = \frac{1}{hA} \end{cases} \tag{6}$$

The parameters used in the thermal model calculation formulas are listed in Table S2.

The temperature sensors arranged in the power battery system of the real vehicle can measure the battery shell temperature. Hence, the deviation between the measurement shell temperature of the sensors and the estimated shell temperature of the model can be used to close-loop correct the estimated battery core temperature, so the EKF algorithm is applied here for closed-loop temperature estimation. The EKF algorithm here is consistent with that used in the aforementioned SOC estimation; the specific definition and calculation process are detailed in the supplementary file.

2.2.2. Thermal Resistance Network of Battery System

Based on the single-cell thermal model, the heat transfer and heat dissipation processes between cells to cells and cells to the environment are abstracted into thermal resistances, which can be connected into a battery pack thermal model. The lumped parameters thermal model of the battery module proposed in this study has both high accuracy and low complexity; thus, it is suitable for estimating the cell temperature in real-time BMS application.

The structure of the battery pack modeled in this study is shown in Figure 2b. The red dots represent the temperature sensor placement sites. It can be seen that it is composed of 4 modules in series, each module is in a structure of eight cells in series, showing a high degree of symmetry as a whole, and there are in total eight temperature sensors in the pack, which is far less than the number of single cells.

The connection between single shells and between shells and the environment is modeled by thermal resistance; the expression is shown in Equation (7): where T_b is the bottom plate temperature, R_{s2b} is the thermal resistance between the shell and bottom plate, T_a is the ambient air temperature, R_{s2a} is the thermal resistance between the shell and ambient air, T_{next} is the adjacent battery shell temperature, and R_{next} is the thermal resistance between the two battery shells.

$$c_s \frac{\Delta T_s}{\Delta t} = \frac{T_{core} - T_s}{R_{core2s}} - \frac{T_s - T_b}{R_{s2b}} - \frac{T_s - T_a}{R_{s2a}} - \frac{T_s - T_{next}}{R_{next}} \tag{7}$$

For each single cell, the heat source is the core, and the heat goes to the bottom plate, the ambient air, and the adjacent cells. According to the symmetry of the pack, the cells in the battery pack are divided into four groups, as shown in Figure 3. The heat transfer paths of the cells in the same region are the same, and the heat transfer paths of different regions are different. To reduce computation, half of the battery pack is modeled in the study, and another half pack is considered to be completely symmetrical.

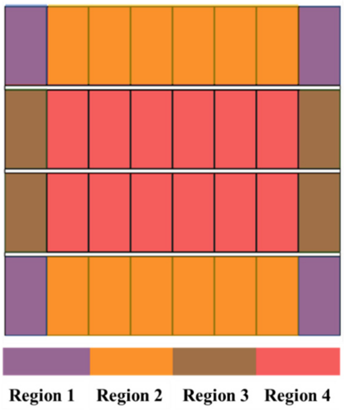

Figure 3. The four regions defined in the battery pack according to symmetry.

3. Experiments

3.1. Experiment Set-Up and Battery Electrical Model Parameter Identification

The object of this study is an LFP prismatic cell manufactured by Ruipu Energy Co., Ltd. of China (Ruipu Energy Co., Ltd., Wenzhou, China). It is the cell assembled on Wuling HongGuang Mini EV. The standard capacity is 135 Ah, and the cut-off voltage of discharge and charge process are 2.5 V (above 0 °C) /2.0 V (below 0 °C) and 3.65 V, respectively. The configuration of the test bench is shown in Figure 4. A Neware CT-8000 battery test system (Neware Technology Co., Ltd., Shenzhen, China) is used to control the charge/discharge process while monitoring the voltage and current, a Bell BE-THK incubator (Guangdong Bell Experiment Equipment Co., Ltd., Dongguan, China) was used to obtain various test temperatures, and K-type thermal couples are used in cooperation with a Pico TC-08 data recorder to monitor the battery temperature.

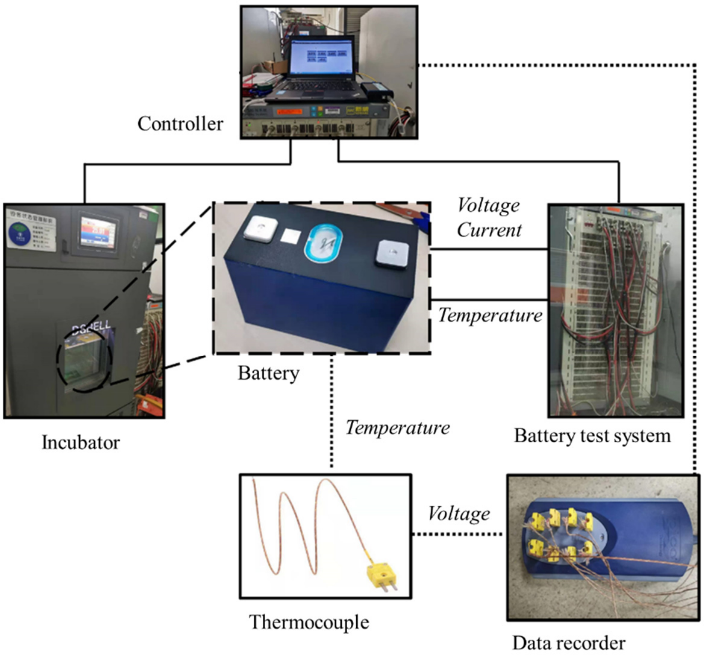

Figure 4. The configuration of the test bench.

To identify the parameters in ECM, an HPPC test is conducted under various temperatures [46]. Charge and discharge pulse currents are applied at different SOCs, and the optimal parameters are obtained by the least squares fitting method of the battery voltage response. To avoid lithium plating during charging at temperatures below zero, only a discharge pulse is applied at subzero temperatures. The HPPC test protocol is shown in Figure 5a,b; the identified parameters of ECM are shown in Figure 5c–h, and the significant increase in the battery's resistance at low temperature is indicated.

Training the neural network requires a lot of dynamic data. This study uses NEDC and FUDS dynamic test conditions, and it selects seven long-term and continuous current data from the real vehicle data set of a vehicle tested in winter of Beijing at year 2020 [8], respectively, to form a data set. All the current protocols are shown in Figure 6. In Figure 6h,i, it can be seen that at subzero temperatures, the battery system no longer recovers braking energy.

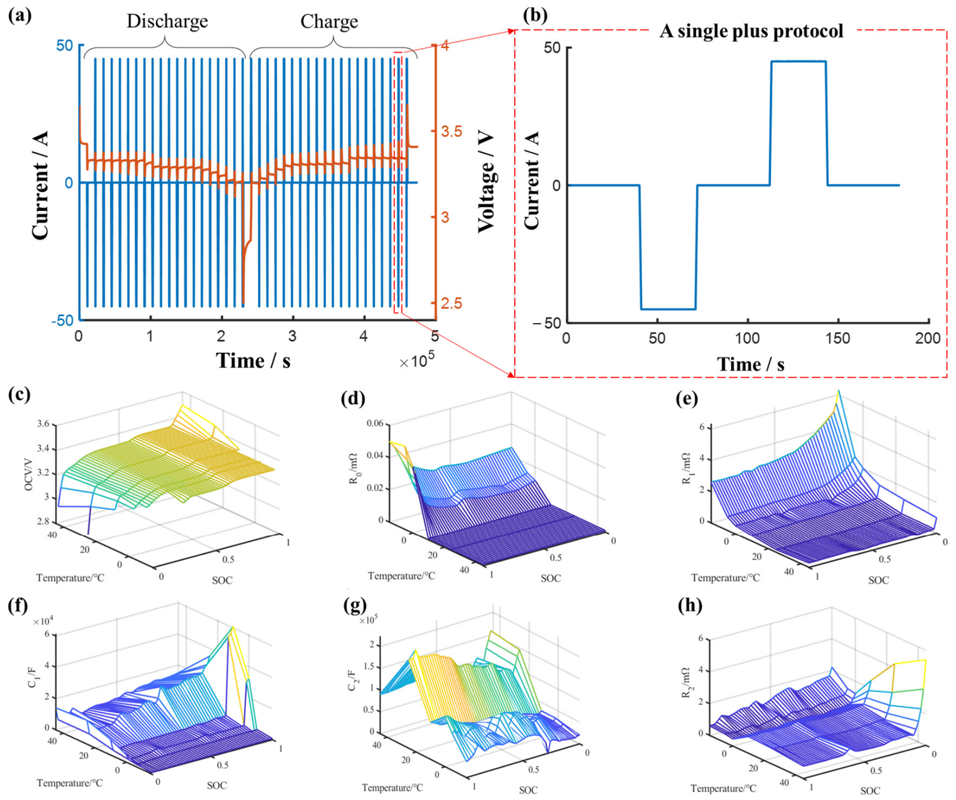

Figure 5. The HPPC test protocol and identified parameters of ECM. (**a**) Full protocol of the HPPC test. (**b**) A single plus protocol. (**c**) The identified OCV. (**d**) The identified R0. (**e**) The identified R1. (**f**) The identified C1. (**g**) The identified C2. (**h**) The identified R2.

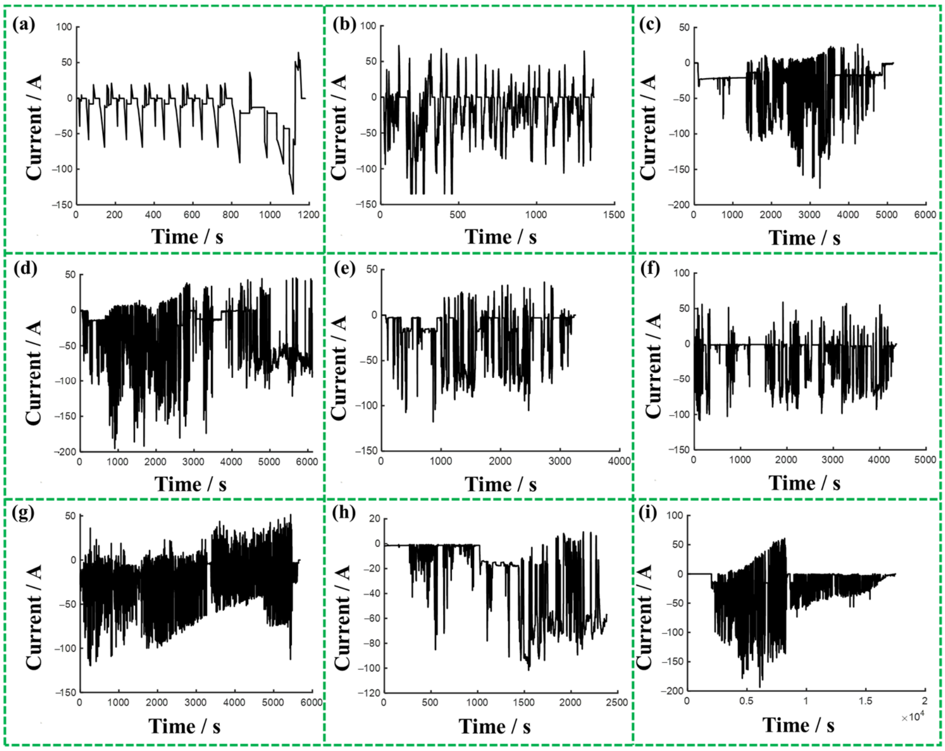

Figure 6. The current protocols used in NN training and validation. (**a**) NEDC operating condition. (**b**) FUDS operating condition. (**c**)–(**i**) Dynamic operating conditions selected from real vehicle data.

In order to ensure the generalization performance of the training set, two batteries are used in the testing process, and the above current conditions are randomly combined for continuous dynamic testing. Tests were carried out at −16 °C, −8 °C, 0 °C, 10 °C and 25 °C, respectively. During testing, thermocouples were used to measure the temperature of the battery case, which is one of the neural network inputs. Use the data of battery 1 as the training set and the data of battery 2 as the validation set to evaluate the accuracy of the model. The estimated results of the terminal voltage on the training set and the validation set are shown in Figure S5. The RMSE of the training set is 3.4 mV, while the RMSE of the validation set is 4.2 mV; these can both reflect the high accuracy of the NN model.

3.2. Experiments to Verify the Battery Thermal Model

Experiments are conducted to verify the thermal model of the cell. To accurately monitor the core temperature of the battery, this study applied an internal-installed thermocouple [47]; the detailed operating procedures are shown in Figure S6.

Charge and discharge experiments are carried out under 1/3 C at 25 °C. The results are shown in Figure 7a. The blue solid line is the shell temperature, and the blue dotted line is the core temperature. During the whole measurement process, the maximum temperature difference between the core and the shell is about 4 °C, which confirms that the lumped thermal model abstracting the cell into a core and a shell is necessary.

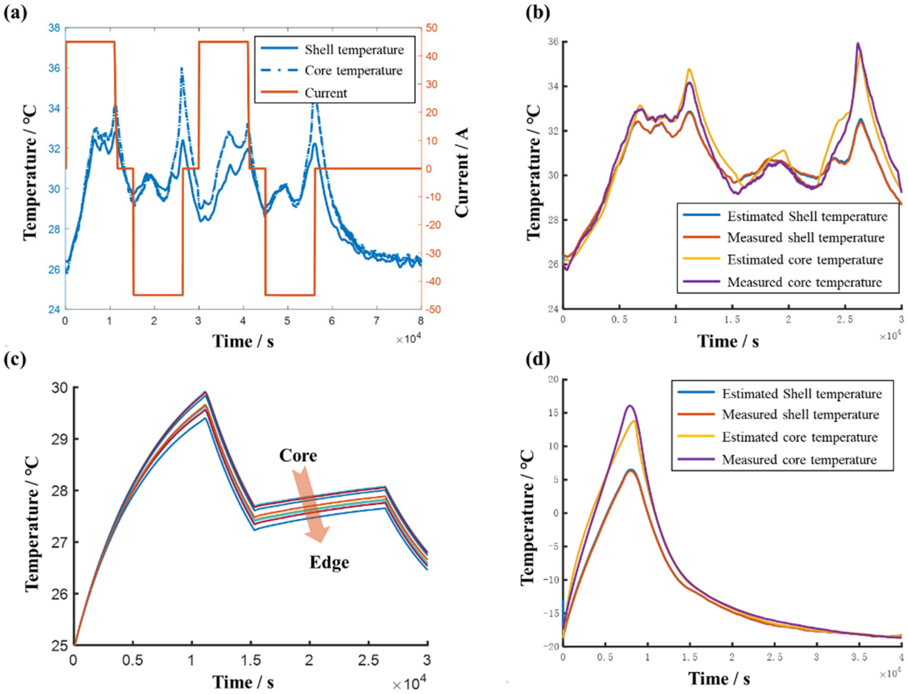

Figure 7. The experiment and simulation results of the thermal model. (**a**) Temperature measurement experiment results at 25 °C. (**b**) The validation of a single battery model at 25 °C. (**c**) Simulation results of the module model. (**d**) The validation of a single battery model at −20 °C.

Experiments at various temperatures are further carried out to validate the battery thermal model. The validation results are shown in Section 4.

4. Results and Discussion

The thermal state and electrical state of the battery show a strong coupling relationship. Temperature change will cause change of the parameters in the battery electric model, which will affect the SOC estimation process. SOC change will cause the change of internal resistance and entropy thermal coefficient, which will affect the heat production of the thermal model. Therefore, in the simulation process, the thermal state of the batteries is co-estimated with SOC.

4.1. Battery SOC Estimation Results

4.1.1. Battery Thermal State Estimation Results

Using the experimental data at room temperature of 25 °C and low temperature of −20 °C, the closed-loop model accuracy is verified, as shown in Figure 7b,d. The RMSE between the simulated core value and the measured core value, and its proportion of the whole temperature rise range, are shown in Table 1.

Table 1. The simulation results of the cell thermal model.

Ambient Temperature/°C	RMSE/°C	Proportion of the Whole Temperature Rise Range/%
25	0.4616	5.13
−20	0.8795	2.67

Then, the battery pack model is simulated, and the results of the 25 °C and 1/3 C simulation are shown in Figure 7c. It can be seen that during cycling, different cells in the battery module have obvious temperature differences.

4.1.2. Closed-Loop EKF SOC Estimation Algorithm

With the battery model using current, initial parameters and environment parameters as input, the battery terminal voltage can be calculated. The EKF algorithm is then used to make a closed-loop estimation of SOC [48]. The algorithm logic diagram is shown in Figure 8a, and the specific calculation process is shown in Figure 8b, which is also the integral SOC estimating process of ECM. In the feedforward process, the prior estimated SOC is obtained with the Coulomb counting method; then, Kalman gain is calculated. In the feedback process, the deviation between the measured terminal voltage and model output terminal voltage is obtained to make a modification of the prior estimated SOC and obtain the posterior estimated SOC.

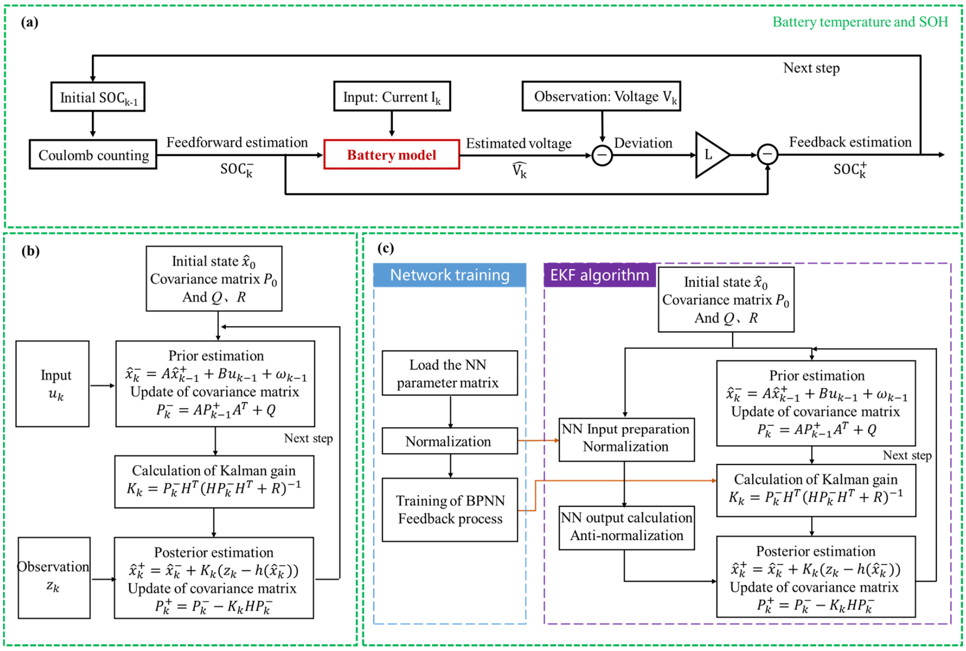

Figure 8. The EKF algorithm in estimating battery SOC. (**a**) The algorithm logic diagram. (**b**) The specific calculation process based on ECM. (**c**) The specific calculation process based on NN model.

It is worth illustrating that in an attempt to improve the training effect of NN, the input data are first normalized, which have an influence on the calculation of Kalman gain and posterior estimation. The integral SOC estimating process of NN is shown in Figure 8c. The main difference between the EKF algorithm of ECM and the NN model is the battery model used in the feedforward process and Kalman gain in the feedback process. In the NN-based algorithm, to obtain the Kalman gain K_k, the measurement observation matrix H is calculated, which is the partial derivative of output z over input x, as shown in Equation (8):

$$H_k = \frac{\partial z_k}{\partial x_k} = W_2 * \left(\left(W_1 * [0,1,0,1]^T\right) * \left([1;\ldots;1]_{6\times 1} - tansig(b_1)\,\hat{}\,2\right)\right) \tag{8}$$

4.1.3. Revisiting the LFP SOC Estimation Task and Fusion Method

We return once more to the LFP SOC estimation task. The NN model is carried out to avoid the platform problem of the LFP OCV curve, but it also brings a higher amount of computation and higher potential instability, which is unfriendly to the practical use of BMS. Since the ECM method is capable of SOC estimation in the non-platform area, this study designs a fusion method for estimating the SOC in segments by the ECM model and the NN model. In the platform area, the NN model is used to estimate the SOC, while in the non-platform area, the ECM model is used to conduct estimation. The combination method is shown in Figure S7. This method is a tradeoff between the accuracy, complexity and stability.

4.1.4. Battery SOC Estimation Results and Discussion

The three SOC estimation methods are compared under NEDC test condition. Three different common error sources [49] are set up to compare the accuracy of the algorithms, which are: the initial SOC has 5% error, the capacity has 5% error and the current has 5% error. The results are shown in Figure 9.

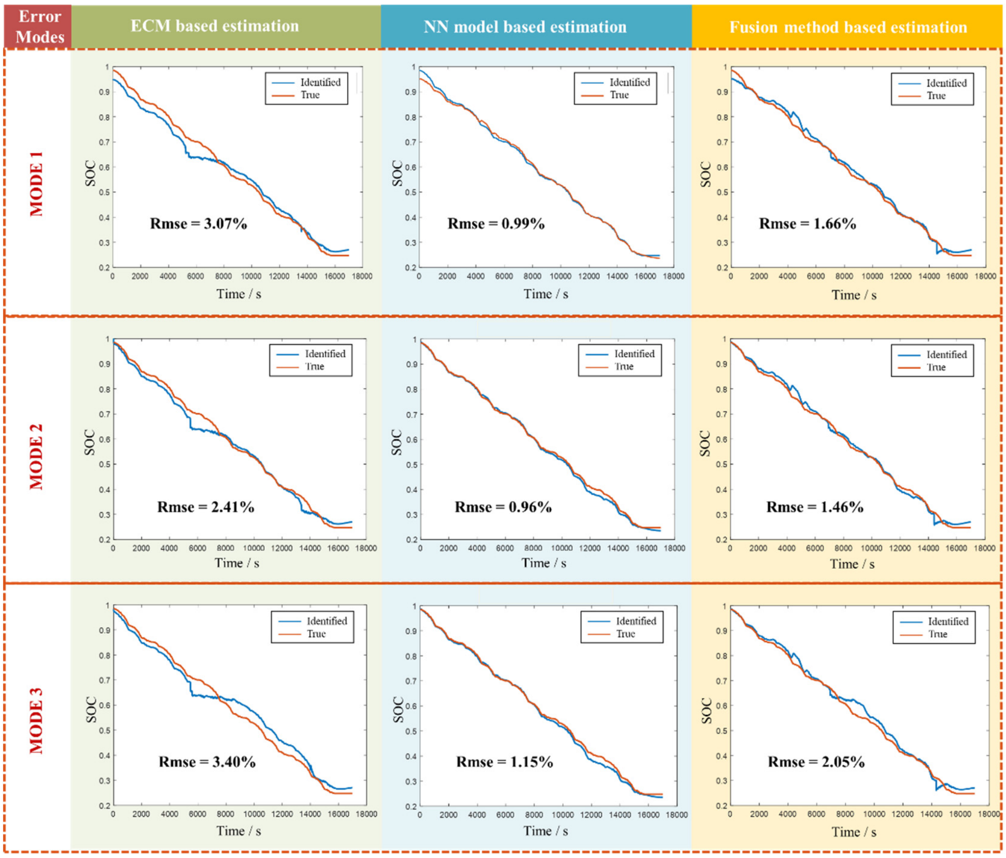

Figure 9. The SOC estimation results of different algorithms under three error modes.

According to the result curves and RMSE of different algorithms, the ECM-based method has no correction effect in the platform areas and thus has the lowest accuracy, while the NN-based method can make corrections through the whole process and has the highest accuracy, and the fusion method has a similar effect to the NN method and has a high accuracy.

Since it is difficult for the data set used to train the NN model to cover all working conditions, it is impossible to determine whether it will suddenly fail due to strange working conditions one day in the future, which will cause very serious consequences. Therefore, it is not appropriate to apply the pure NN algorithm to the real vehicle BMS independently. The fusion method proposed in the study has a similar accuracy to the NN method, and it can ensure that there will be a closed-loop algorithm based on the ECM to correct the estimated SOC in the non-platform area, thus ensuring its stability in the whole process, so it is a more applicable SOC estimation method in the authors' view.

4.2. Operation Condition-Based RAE Calculation Algorithm

The RAE of the battery module is calculated by the integral Equation (9):

$$E_{RAE}\,|_{I,T,\mathrm{SOC},SOH} = \int_{t_0}^{t_{end}} U_{out} \cdot I \cdot dt \tag{9}$$

where t_{end} is the time when the battery terminal voltage reaches the low limit cut-off voltage.

Ren et al. introduced an approach to estimate the battery remaining discharge energy by predicting the future operating conditions [50], which has been imitated by the subsequent studies [51,52], but few researchers have paid attention to the temperature and SOC difference among batteries in the module, which is a big influence factor of the battery module RAE especially in low temperatures because of "short board effect". Taking advantage of the SOC estimation method and battery module thermal model, this study conducted an operation condition-based RAE estimation method of the LFP battery module; thus, the estimation accuracy is further improved. While this study does not involve the extraction and prediction of operating conditions, the WLTC test condition is used as the operation condition in the simulation, according to the Chinese industry test standards. The operation conditions prediction methods can be equally applied in this model.

The total process of SOC and temperature co-estimation and calculation of RAE is shown in Figure 10a, and the detailed flow chart of RAE calculation is shown in Figure 10b. When the temperature of any single cell in the series battery system is lower than 0 °C, the brake energy feedback is turned off and the charge current will be turned to zero; when the voltage of any cell in the system reaches the cut-off voltage, the whole discharge process is cut off, and the calculation is stopped. The sum of the discharge energy of the cells is the RAE of the module under WLTC test condition.

The real vehicle dynamic operating condition data extracted in Section 2 are used to validate the RAE calculation. The ambient temperature is obtained by checking the local history of that day. The initial SOC, initial module temperature and actual discharge energy until cut-off voltage are obtained by the data recorded of BMS. Although the actual driving condition is not the WLTC condition, the WLTC condition is still representative of the urban driving protocol. The parameters and results are shown in Table 2. The results demonstrate the validity of the RAE calculation method and the representativeness of the operating conditions.

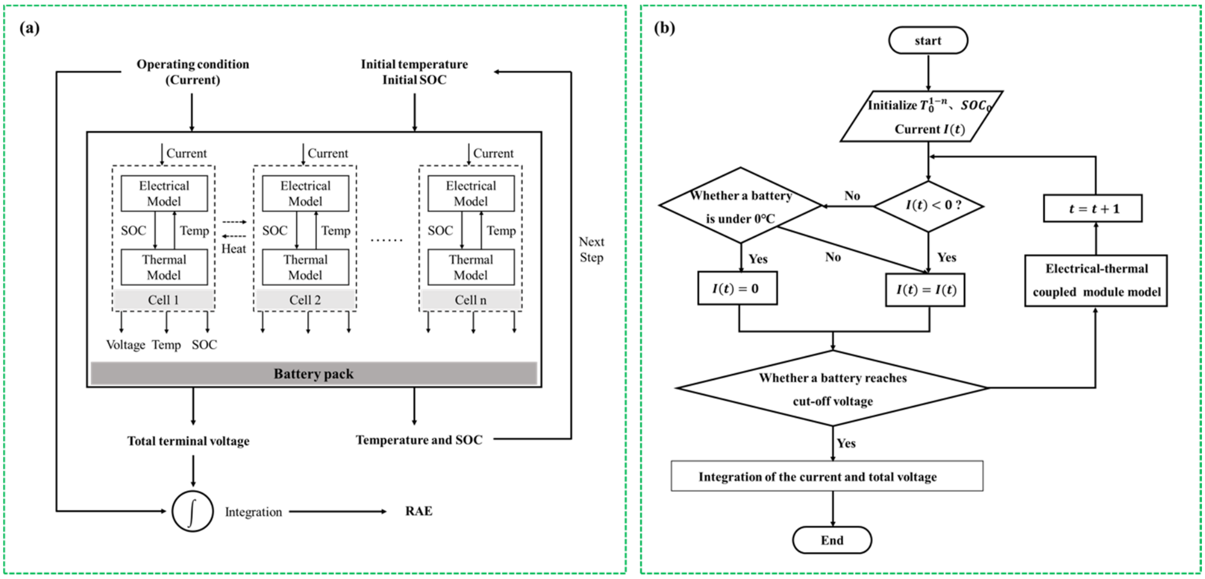

Figure 10. The calculation process of RAE. (**a**) Total process of SOC and temperature co-estimation and calculation of RAE. (**b**) Detailed flow chart of RAE calculation.

Table 2. The parameters of the validation condition and results.

Parameter	Value
Initial SOC	50%
Ambient temperature	−10 °C
RAE from simulation	6.606 kWh
Real RAE	6.363 kWh
Estimation error	+3.82%

4.3. Energy Recovery Effect under Heating Strategy

4.3.1. Heating Strategy

The battery preheating at low temperature is one way to increase available energy [8]. On the one hand, raising the temperature can lower the battery resistance and obtain energy recovery; on the other hand, heating the battery consumes the energy contained in the battery, so there is a trade-off relationship. This study assumes preheating the battery per 1°C consumes 0.15% SOC [8], and we calculated the RAE with/without heating.

For a better comparison, the SOE of the battery module is obtained by normalizing the RAE to the total discharge energy from a fully charged state to a completely discharged state without heating. The SOE values at ambient temperature of −20 °C, −15 °C, −10 °C and −5 °C are calculated, respectively, under the WLTC operating current, and starting from no preheating, the preheat temperatures are set every 5 °C. The results are shown in Figure 11. It can be seen that the heating strategy has a significant effect on the energy recovery at low temperatures and low SOC, while at high SOC, heating would lower the total energy, which is because the battery module has strong self-heating capacity.

4.3.2. RAE Prediction under Constant Power Condition

Expect for the WLTC operating condition, another RAE generation strategy is based on constant power discharge. Compared with the WLTC condition, this strategy can batter reflect the drivers' characteristics and the specific average driving conditions.

Applying the big data, or historical output power, or assisted driving app for calculation, an average output power can be obtained of the specific driving state, and based on the look-up table generated in advance, the RAE can be obtained directly without calculation, which is applicable to BMS.

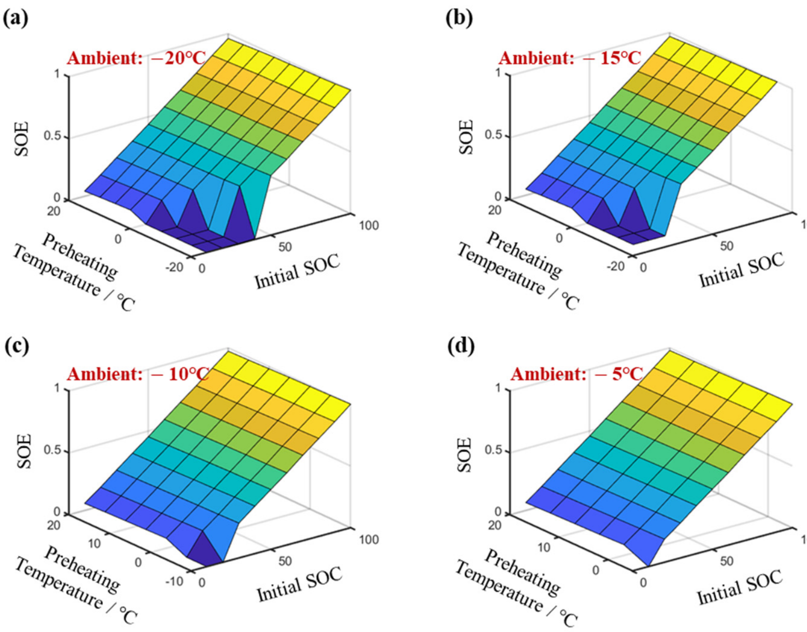

Figure 11. The effect of preheating to energy state at various low temperatures. (**a**) Ambient temperature and battery initial temperature is −20 °C. (**b**) Ambient temperature and battery initial temperature is −15 °C. (**c**) Ambient temperature and battery initial temperature is −10 °C. (**d**) Ambient temperature and battery initial temperature is −5 °C.

The constant power condition-based RAE calculating process is as follows: first, the optional current is calculated according to the power and the optional voltage, and then, the voltage at the next time step is calculated according to the optional current. Solve iteratively until the cut-off voltage is reached, and the total discharge energy is obtained by the product of power and total time. At ambient temperature of −20 °C, RAE calculations are performed at a constant output power of 1.5, 2.0, 3.0 and 4.0 kW with preheating to different temperatures. The results are shown in Figure 12.

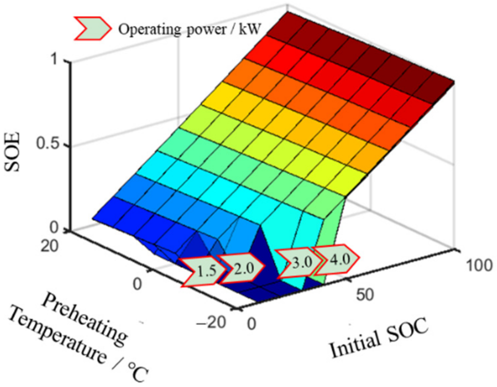

Figure 12. SOE of the module discharged at different constant powers at −20 °C and with preheating.

It can be seen that with the increase in discharge power, the RAE of the battery gradually decreases, and this phenomenon is more obvious at low SOC. The conclusion is: the preheating strategy at low temperature and low SOC can significantly improve the driving range, and the demand for preheating is greater at higher power output.

5. Conclusions

Aiming at relieving the mileage anxiety of LFP-assembled EVs, this study focuses on the precise estimation of SOC and RAE for LFP battery, especially in low temperature. An EKF algorithm is conducted with an NN battery model to calculate the SOC estimation, which can avoid the LFP battery voltage plateau problems compared with traditional methods. Furthermore, the fusion method using the NN model in the voltage plateaus, and ECM in the non-plateaus area is carried out to increase the robustness of the algorithm. A thermal resistance network of the battery module is built based on a two-state lumped parameter battery thermal model, and the temperature distribution of the module can be closed-loop calculated with limited temperature sensors. The WLTC operating condition is applied in the simulation of the module model, and RAE is obtained. Finally, the preheating method and constant power condition-based RAE estimation are discussed to optimize BMS application. The main conclusions are listed as follows:

(1) The ECM-based LFP battery SOC estimation method has barely any correction effect in the plateaus areas, while the NN-based method can effectively correct the estimation result with the highest accuracy, and the fusion method has a similar effect to the NN method and has a high accuracy. Considering accuracy, complexity and robustness, the fusion method is preferred in the LFP SOC estimation process, and the SOC estimation error can be controlled within 2%.

(2) The temperature inconsistency inside the battery system would obviously influence the battery discharge capability, and the proposed two-state battery thermal model shows a good performance in estimating the system temperature distribution; thus, it can improve the RAE estimation accuracy, and the error of the WLTC operating condition-based RAE prediction method is below 4%.

(3) The preheating strategy at low temperature and low SOC can significantly improve the driving range, and the required preheating power is greater at a higher power output demand.

The full set of methods proposed in this study is also applicable to batteries of other material systems in the full temperature range. In the future, the authors will focus on introducing other dimensional signals to improve the accuracy and reliability of LFP battery SOC estimation as well as proposing more effective operating condition prediction methods to improve the RAE estimation accuracy. In addition, the research did not involve the degradation of the battery, which should be considered in real BMS application. The automatic update method of the capacity and resistance is being researched by the authors.

Supplementary Materials: The following are available online at https://www.mdpi.com/article/10.3390/batteries8100140/s1, Figure S1: Discharge experiments under normal temperature and low temperatures, Figure S2: The OCV-SOC curve of LFP battery at 25 °C and the three platform areas, Figure S3: The terminal voltage under dynamic conditions of LFP battery, Figure S4: The maps of heat production parameters, Figure S5: The estimated results of the terminal voltage on the training dataset and the validation dataset, Figure S6: The detailed operating procedures of inserting thermocouple into the battery, Figure S7: The combination method of the two models, Table S1: The basic thermal parameters of the core and shell, Table S2: The parameters used in the thermal model calculation formulas.

Author Contributions: Conceptualization, S.M. and M.H.; methodology, S.M. and M.H.; software, S.M.; validation, S.M.; formal analysis, S.M.; investigation, S.M.; resources, S.M.; data curation, S.M. and M.H.; writing—original draft preparation, S.M.; writing—review and editing, S.M., M.H. and X.H.; visualization, S.M.; supervision, X.H., L.L., X.F. and M.O.; project administration, X.H. and L.L.; funding acquisition, Y.L., A.S., Z.C. and D.W. All authors have read and agreed to the published version of the manuscript.

Funding: This paper is supported by the National Key R&D Program of China (No. 2021YFB2401901), China Postdoctoral Science Foundation (No. 2021M691729), Beijing Science and Technology Planning Project (No. Z211100004221011), National Natural Science Foundation of China (No. 52177217 and No. 52037006), Beijing Natural Science Foundation (No. 3212031), Tsinghua-Toyota Joint Research Fund (No. 20213930025).

Institutional Review Board Statement: Not applicable.

Informed Consent Statement: Not applicable.

Data Availability Statement: Not applicable.

Acknowledgments: The authors thank Ruipu Energy Co., Ltd.; KeyPower Technologies Co., Ltd.; and SAIC GM Wuling Co., Ltd., for providing technical documentation and data.

Conflicts of Interest: The authors declare no conflict of interest.

References

1. Fachrizal, R.; Shepero, M.; van der Meer, D.; Munkhammar, J.; Widén, J. Smart charging of electric vehicles considering photovoltaic power production and electricity consumption: A review. *eTransportation* **2020**, *4*, 100056. [CrossRef]
2. Lu, Y.; Han, X.; Chu, Z.; Feng, X.; Qin, Y.; Ouyang, M.; Lu, L. A decomposed electrode model for real-time anode potential observation of lithium-ion batteries. *J. Power Source* **2021**, *513*, 230529. [CrossRef]
3. Feng, X.; Merla, Y.; Weng, C.; Ouyang, M.; He, X.; Liaw, B.Y.; Santhanagopalan, S.; Li, X.; Liu, P.; Lu, L.; et al. A reliable approach of differentiating discrete sampled-data for battery diagnosis. *eTransportation* **2020**, *3*, 100051. [CrossRef]
4. Lu, Y.; Li, K.; Han, X.; Feng, X.; Chu, Z.; Lu, L.; Huang, P.; Zhang, Z.; Zhang, Y.; Yin, F.; et al. A method of cell-to-cell variation evaluation for battery packs in electric vehicles with charging cloud data. *eTransportation* **2020**, *6*, 100077. [CrossRef]
5. Riviere, E.; Sari, A.; Venet, P.; Meniere, F.; Bultel, Y. Innovative Incremental Capacity Analysis Implementation for C/LiFePO4 Cell State-of-Health Estimation in Electrical Vehicles. *Batteries* **2019**, *5*, 37. [CrossRef]
6. Mauger, A.; Julien, C.M. Olivine Positive Electrodes for Li-Ion Batteries: Status and Perspectives. *Batteries* **2018**, *4*, 39. [CrossRef]
7. Steinstraeter, M.; Buberger, J.; Minnerup, K.; Trifonov, D.; Horner, P.; Weiss, B.; Lienkamp, M. Controlling cabin heating to improve range and battery lifetime of electric vehicles. *eTransportation* **2022**, *13*, 100181. [CrossRef]
8. Mao, S.; Han, M.; Han, X.; Shao, J.; Lu, Y.; Lu, L.; Ouyang, M. Analysis and Improvement Measures of Driving Range Attenuation of Electric Vehicles in Winter. *World Electr. Veh. J.* **2021**, *12*, 239. [CrossRef]
9. Qin, P.; Sun, J.; Yang, X.; Wang, Q. Battery thermal management system based on the forced-air convection: A review. *eTransportation* **2020**, *7*, 100097. [CrossRef]
10. Piao, N.; Gao, X.; Yang, H.; Guo, Z.; Hu, G.; Cheng, H.-M.; Li, F. Challenges and development of lithium-ion batteries for low temperature environments. *eTransportation* **2021**, *11*, 100145. [CrossRef]
11. Zheng, L.; Zhang, L.; Zhu, J.; Wang, G.; Jiang, J. Co-estimation of state-of-charge, capacity and resistance for lithium-ion batteries based on a high-fidelity electrochemical model. *Appl. Energy* **2016**, *180*, 424–434. [CrossRef]
12. Wu, L.; Liu, K.; Pang, H. Evaluation and observability analysis of an improved reduced-order electrochemical model for lithium-ion battery. *Electrochim. Acta* **2021**, *368*, 137604. [CrossRef]
13. Liu, Y.; Ma, R.; Pang, S.; Xu, L.; Zhao, D.; Wei, J.; Huangfu, Y.; Gao, F. A Nonlinear Observer SOC Estimation Method Based on Electrochemical Model for Lithium-Ion Battery. *IEEE Trans. Ind. Appl.* **2020**, *57*, 1094–1104. [CrossRef]
14. Mahfoudi, N.; Boutaous, M.; Xin, S.; Buathier, S. Thermal Analysis of LMO/Graphite Batteries Using Equivalent Circuit Models. *Batteries* **2021**, *7*, 58. [CrossRef]
15. Liu, Y.; Liu, Y.; Zhang, C.; Jiang, J.; Zhang, L.; Zhang, W. Deduction of the transformation regulation on voltage curve for lithium-ion batteries and its application in pa-rameters estimation. *eTransportation* **2022**, *12*, 100164. [CrossRef]
16. Kim, J.; Kowal, J. Development of a Matlab/Simulink Model for Monitoring Cell State-of-Health and State-of-Charge via Impedance of Lithium-Ion Battery Cells. *Batteries* **2022**, *8*, 8. [CrossRef]
17. Wang, X.; Wei, X.; Zhu, J.; Dai, H.; Zheng, Y.; Xu, X.; Chen, Q. A review of modeling, acquisition, and application of lithium-ion battery impedance for onboard battery management. *eTransportation* **2021**, *7*, 100093. [CrossRef]
18. Baronti, F.; Femia, N.; Saletti, R.; Visone, C.; Zamboni, W. Hysteresis Modeling in Li-Ion Batteries. *IEEE Trans. Magn.* **2014**, *50*, 7300704. [CrossRef]
19. Duong, V.-H.; Bastawrous, H.; See, K. Accurate approach to the temperature effect on state of charge estimation in the LiFePO4 battery under dynamic load operation. *Appl. Energy* **2017**, *204*, 560–571. [CrossRef]
20. Li, J.; Barillas, J.K.; Guenther, C.; Danzer, M.A. A comparative study of state of charge estimation algorithms for LiFePO4 batteries used in electric vehicles. *J. Power Source* **2013**, *230*, 244–250. [CrossRef]
21. Xiong, R.; Li, L.; Yu, Q.; Jin, Q.; Yang, R. A set membership theory based parameter and state of charge co-estimation method for all-climate batteries. *J. Clean. Prod.* **2020**, *249*, 119380. [CrossRef]
22. Chen, C.; Xiong, R.; Yang, R.; Shen, W.; Sun, F. State-of-charge estimation of lithium-ion battery using an improved neural network model and extended Kalman filter. *J. Clean. Prod.* **2019**, *234*, 1153–1164. [CrossRef]
23. Song, Z.; Yang, X.-G.; Yang, N.; Delgado, F.P.; Hofmann, H.; Sun, J. A study of cell-to-cell variation of capacity in parallel-connected lithium-ion battery cells. *eTransportation* **2021**, *7*, 100091. [CrossRef]
24. Ludwig, S.; Steinhardt, M.; Jossen, A. Determination of Internal Temperature Differences for Various Cylindrical Lithi-um-Ion Batteries Using a Pulse Resistance Approach. *Batteries* **2022**, *8*, 60. [CrossRef]
25. Wildfeuer, L.; Lienkamp, M. Quantifiability of inherent cell-to-cell variations of commercial lithium-ion batteries. *eTransportation* **2021**, *9*, 100129. [CrossRef]
26. Lin, X. Adaptive Estimation of Thermal Dynamics and Charge Imbalance in Battery Strings. Ph.D. Thesis, University of Michigan, Ann Arbor, MI, USA, 2014.

27. Feng, X.; Weng, C.; Ouyang, M.; Sun, J. Online internal short circuit detection for a large format lithium ion battery. *Appl. Energy* **2016**, *161*, 168–180. [CrossRef]
28. Zhang, F.; Feng, X.; Xu, C.; Jiang, F.; Ouyang, M. Thermal runaway front in failure propagation of long-shape lithium-ion battery. *Int. J. Heat Mass Transf.* **2022**, *182*, 121928. [CrossRef]
29. Hua, X.; Heckel, C.; Modrow, N.; Zhang, C.; Hales, A.; Holloway, J.; Jnawali, A.; Li, S.; Yu, Y.; Loveridge, M.; et al. The prismatic surface cell cooling coefficient: A novel cell design optimisation tool & thermal parameterization method for a 3D discretised electro-thermal equivalent-circuit model. *eTransportation* **2021**, *7*, 100099. [CrossRef]
30. Jiang, Z.Y.; Qu, Z.G.; Zhang, J.F.; Rao, Z.H. Rapid prediction method for thermal runaway propagation in battery pack based on lumped thermal re-sistance network and electric circuit analogy. *Appl. Energy* **2020**, *268*, 115007. [CrossRef]
31. Cui, X.; Zeng, J.; Zhang, H.; Yang, J.; Qiao, J.; Li, J.; Li, W. Optimization of the lumped parameter thermal model for hard-cased li-ion batteries. *J. Energy Storage* **2020**, *32*, 101758. [CrossRef]
32. Li, K.; Tseng, K.J. An equivalent circuit model for state of energy estimation of lithium-ion battery. In Proceedings of the Apec 2016 31st Annual IEEE Applied Power Electronics Conference and Exposition, Long Beach, CA, USA, 20–24 March 2016; pp. 3422–3430. [CrossRef]
33. Dong, T.K.; Montaru, M.; Kirchev, A.; Perrin, M.; Lambert-Mattera, F.; Bultel, Y. Modeling of Lithium Iron Phosphate Batteries by an Equivalent Electrical Circuit: Part II-Model Parame-terization as Function of Power and State of Energy (SOE). *ECS Trans.* **2011**, *35*, 229–237. [CrossRef]
34. Dong, G.; Chen, Z.; Wei, J.; Zhang, C.; Wang, P. An online model-based method for state of energy estimation of lithium-ion batteries using dual filters. *J. Power Source* **2016**, *301*, 277–286. [CrossRef]
35. Mamadou, K.; Delaille, A.; Lemaire-Potteau, E.; Bultel, Y. The State-of-Energy: A New Criterion for the Energetic Performances Evaluation of Electrochemical Storage Devices. *ECS Trans.* **2010**, *25*, 105–112. [CrossRef]
36. Li, K.; Wei, F.; Tseng, K.J.; Soong, B.-H. A Practical Lithium-Ion Battery Model for State of Energy and Voltage Responses Prediction Incorporating Temperature and Ageing Effects. *IEEE Trans. Ind. Electron.* **2018**, *65*, 6696–6708. [CrossRef]
37. Wang, Y.; Zhang, C.; Chen, Z. A method for joint estimation of state-of-charge and available energy of LiFePO 4 batteries. *Appl. Energy* **2014**, *135*, 81–87. [CrossRef]
38. Zhang, S.; Zhang, X. A novel non-experiment-based reconstruction method for the relationship between open-circuit-voltage and state-of-charge/state-of-energy of lithium-ion battery. *Electrochim. Acta* **2021**, *403*, 139637. [CrossRef]
39. Zhang, Y.Z.; He, H.W.; Xiong, R. A Data-Driven Based State of Energy Estimator of Lithium-ion Batteries Used to Supply Electric Vehicles. *Energy Procedia* **2015**, *75*, 1944–1949. [CrossRef]
40. Li, K.; Soong, B.H.; Tseng, K.J. A High-Fidelity Hybrid Lithium-Ion Battery Model for SOE and Runtime Prediction. In Proceedings of the 2017 Thirty Second Annual IEEE Applied Power Electronics Conference and Exposition (APEC), Tampa, FL, USA, 26–30 March 2017; pp. 2374–2381.
41. Zhang, S.; Peng, N.; Zhang, X. An application—Oriented multistate estimation framework of lithium—Ion battery used in electric vehicles. *Int. J. Energy Res.* **2021**, *45*, 18554–18576. [CrossRef]
42. Zhang, S.; Zhang, X. Joint estimation method for maximum available energy and state-of-energy of lithium-ion battery under various temperatures. *J. Power Source* **2021**, *506*, 230132. [CrossRef]
43. Liu, X.; Wu, J.; Zhang, C.; Chen, Z. A method for state of energy estimation of lithium-ion batteries at dynamic currents and temperatures. *J. Power Source* **2014**, *270*, 151–157. [CrossRef]
44. German, R.; Shili, S.; Desreveaux, A.; Sari, A.; Venet, P.; Bouscayrol, A. Dynamical Coupling of a Battery Electro-Thermal Model and the Traction Model of an EV for Driving Range Simulation. *IEEE Trans. Veh. Technol.* **2020**, *69*, 328–337. [CrossRef]
45. Tian, J.; Xiong, R.; Shen, W.; Lu, J. State-of-charge estimation of LiFePO4 batteries in electric vehicles: A deep-learning enabled approach. *Appl. Energy* **2021**, *291*, 116812. [CrossRef]
46. Carpenter, J. Freedomcar and Casting. *Int. J. Met.* **2008**, *2*, 7–15. [CrossRef]
47. Jin, C.; Sun, Y.; Wang, H.; Lai, X.; Wang, S.; Chen, S.; Rui, X.; Zheng, Y.; Feng, X.; Wang, H.; et al. Model and experiments to investigate thermal runaway characterization of lithium-ion batteries induced by external heating method. *J. Power Source* **2021**, *504*, 230065. [CrossRef]
48. Shen, P.; Ouyang, M.; Lu, L.; Li, J.; Feng, X. The Co-estimation of State of Charge, State of Health, and State of Function for Lithium-Ion Batteries in Electric Vehicles. *IEEE Trans. Veh. Technol.* **2017**, *67*, 92–103. [CrossRef]
49. Shen, P.; Ouyang, M.; Han, X.; Feng, X.; Lu, L.; Li, J. Error Analysis of the Model-Based State-of-Charge Observer for Lithium-Ion Batteries. *IEEE Trans. Veh. Technol.* **2018**, *67*, 8055–8064. [CrossRef]
50. Ren, D.; Lu, L.; Shen, P.; Feng, X.; Han, X.; Ouyang, M. Battery remaining discharge energy estimation based on prediction of future operating conditions. *J. Energy Storage* **2019**, *25*, 100836. [CrossRef]
51. Sun, T.; Xu, Y.; Feng, L.; Xu, B.; Chen, D.; Zhang, F.; Han, X.; Zhao, L.; Zheng, Y. A vehicle-cloud collaboration strategy for remaining driving range estimation based on online traffic route in-formation and future operation condition prediction. *Energy* **2022**, *248*, 123608. [CrossRef]
52. Lai, X.; Huang, Y.; Gu, H.; Han, X.; Feng, X.; Dai, H.; Zheng, Y.; Ouyang, M. Remaining discharge energy estimation for lithium-ion batteries based on future load prediction considering temperature and ageing effects. *Energy* **2022**, *238*, 121754. [CrossRef]